Self-Assembly of "S-Bilayers", a Step Toward Expanding the Dimensionality of S-Layer Assemblies

Seong-Ho Shin,[†,§,¶,#] Luis R. Comolli,[⊥,#,*] Rupert Tscheliessnig,[‡] Cheng Wang,[∥] Ki Tae Nam,[†,§] Alexander Hexemer,[∥] Cristina E. Siegerist, James J. De Yoreo,[†,§] and Carolyn R. Bertozzi[†,§,¶,*]

[†]Molecular Foundry, Lawrence Berkeley National Laboratory, Berkeley, California 94720, United States, [‡]Austrian Centre for Industrial Biotechnology, Department of Chemical and Biomolecular Engineering, University of California, Berkeley, California 94720, United States, [§]Materials Sciences Division, [⊥]Life Sciences Division, and [∥]Advanced Light Source, Lawrence Berkeley National Laboratory, Berkeley, California 94720, United States, and [¶]Department of Chemistry, University of California, Berkeley, Berkeley, California 94720, United States. [#]These authors contributed equally to this work.

ABSTRACT Protein-based assemblies with ordered nanometer-scale features in three dimensions are of interest as functional nanomaterials but are difficult to generate. Here we report that a truncated S-layer protein assembles into stable bilayers, which we characterized using cryogenic-electron microscopy, tomography, and X-ray spectroscopy. We find that emergence of this supermolecular architecture is the outcome of hierarchical processes; the proteins condense in solution to form 2-D crystals, which then stack parallel to one another to create isotropic bilayered assemblies. Within this bilayered structure, registry between lattices in two layers was disclosed, whereas the intrinsic symmetry in each layer was altered. Comparison of these data to images of wild-type SbpA layers on intact cells gave insight into the interactions responsible for bilayer formation. These results establish a platform for engineering S-layer assemblies with 3-D architecture.

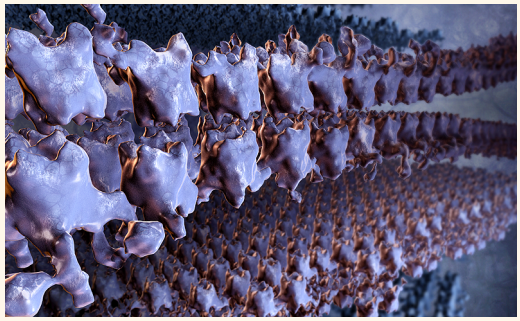

KEYWORDS: cryo-electron microscopy · cryo-electron tomography · S-layers · collective nanostructures · broken symmetry

S-layer proteins form 2-D crystalline lattices on the surfaces of many bacteria and archea. Their highly regular nanometer-scale features, which are readily reproduced *in vitro*, have made S-layer assemblies attractive substrates for nanomaterial engineering.[1] To date, use of S-layer-based assemblies for this purpose has been restricted to applications of 2-D lattices on surfaces, for example, as templates for nanoparticle deposition on surfaces[2−4] or as masks for nanofabrication.[5,6] Though in a recent study, the ability of S-layers to assemble in 2-D on surfaces was exploited to give silica-enhanced S-layer protein cages built from S-layer-coated liposomes.[7] There is growing interest, however, in using protein building blocks to generate true 3-D materials for applications as diverse as catalysis, energy storage, and nanophotonics.[8−10] In the case of S-layers, the inherent ion-selective permeability further underlies the interest in obtaining 3-D reconstructions of intact S-layers with accurate measurements of lattice constants and pore sizes and distributions.[11]

The protein nanoassemblies that have been most widely explored for these applications are viral scaffolds.[12−14] Virus particles offer highly regular nanometer-scale features within the particles themselves but typically form amorphous materials at micrometer scales. In the case of rod-like viruses, the anisotropic shape allows for formation of 3-D liquid crystalline domains, but these domains do not maintain regular lattice structures in 2-D. Consequently, expanding to 3-D structures while keeping nanometer-scale order in 2-D has been a daunting task.

Growth of S-layer assemblies in the third dimension could, in principle, afford protein-based materials with regular nanoporous architectures over longer length scales, an attractive property for numerous applications.[15,16] However, the fast and favorable growth of S-layer crystals in 2-D implies that 3-D crystals are difficult to obtain, and indeed, while stacked S-layers have been observed to form in bacterial systems,[17,18] such structures are difficult to reproduce in

* Address correspondence to crb@berkeley.edu, lrcomolli@lbl.gov.

Received for review January 18, 2013 and accepted May 25, 2013.

Published online May 25, 2013
10.1021/nn400263j

the laboratory. Furthermore, the undulations in S-layers adsorbed on planar lipid bilayers in bulk suspension adds complexity to the behavior of the system.[19] Indeed, only recently was the 3-D growth of an S-layer protein accomplished, and this required alteration of its intrinsic propensity to assemble in 2-D.[20]

Previous works with diverse protein assemblies have shown that novel supramolecular structures can be formed by reprogramming interfaces between protein subunits either directly or through ligand–protein interactions.[21−25] These examples of redesign to achieve higher-order architectures capitalized on a wealth of high-resolution structural data on which to base the careful tailoring of new protein–protein interfaces. In the case of S-layers, however, structural information is limited to low-resolution 2-D electron density maps at 7 Å resolution[26] and topographic images derived from AFM.[27] Only one high-resolution structure is available so far,[20] perhaps reflecting the difficulties inherent to 3-D S-layer protein crystallization.

In 1973, Kellenberger and co-workers noted that, upon limited proteolysis, the 2-D S-layer sheet derived from the *Bacillus brevis* protein underwent a dramatic long-range structural transformation, adopting a non-native cylindrical architecture with specific chirality.[28] More recently, genetic truncations of various S-layer proteins have been shown to alter 2-D lattice parameters.[29] These studies focused on perturbations to S-layer 2-D structure as a consequence of protein subunit truncation, but the possible implications for creation of 3-D arrays were not explored.

Here we report that a truncated form of the S-layer protein derived from *Lysinibacillus sphaericus*, termed SbpA, reproducibly assembles into two types of bilayer structures, providing a first step toward generating 3-D structures. We characterized these bilayers as well as monolayers derived from the same SbpA variant using cryogenic-electron microscopy and tomography (cryo-EM; cryo-ET), producing the highest-resolution 3-D structures of pure S-layers reported to date. Comparison of these data to cryo-ET images of wild-type SbpA crystalline layers on intact cells revealed the molecular orientation of S-layer subunits with respect to the cell surface and gave insight into the interactions responsible for bilayer formation. These results establish a platform for further engineering of S-layer assemblies with 3-D architecture.

RESULTS AND DISCUSSION

Wild-type SbpA naturally forms a 2-D crystalline cell envelope with *p*4 symmetry.[30] *In vitro* reconstitution of disassembled S-layer monomers in the presence of Ca^{2+} ions leads to suspended 2-D crystals with long-range order. Previous work has shown that SbpA, normally a 1268-residue protein, can tolerate C-terminal truncations of up to 200 residues without significant perturbation to its *in vitro* 2-D lattice parameters.[31] SbpA mutants that are further truncated form 2-D lattices with fundamentally altered symmetry or unstructured aggregates.[29] These observations indicate that the 200 C-terminal residues do not critically participate in 2-D lattice interactions. We decided to investigate how the altered chemical nature of the S-layer surface after removal of these residues might change the bulk behavior of these SbpA mutant lattices.

We expressed in *E. coli* a recombinant SbpA variant that substituted the 200 C-terminal residues with a 16-residue epitope tag (termed rSbpA; see Supporting Information for details). The crystallization behavior of the purified rSbpA protein was characterized alongside that of the wild-type (wt) protein isolated from cultured *L. sphaericus* using published protocols.[26] As expected,[32] wt SbpA formed free-standing 2-D crystals (average dimension 1−2 μm) during overnight incubation in 10 mM Tris-HCl pH 7.2 with 50 mM Ca^{2+} at purified protein concentrations of ~1.0 mg/mL (Figure S1). Under the same condition, rSbpA formed small 2-D crystals (~100 nm) with the same symmetry (~13.5 nm lattice constant) but on a much slower time scale (several months) (Figure S1). However, we discovered that the 2-D crystallization process could be dramatically accelerated by centrifugation (4000*g*) of the protein solution with or without Ca^{2+} ions. In less than 30 min, a precipitate formed that light microscopy analysis revealed to be macroscopic protein films (Figure 1a). Atomic force microscopy analysis of this material deposited on a silicon wafer indicated that the film possessed a polycrystalline surface with *p*4 lattice symmetry (Figure S2).

To gain insight into the 3-D structure of the new S-layer material, we performed cryo-EM and cryo-ET analysis of vitreous ice cryo-samples generated by freezing the resuspended rSbpA precipitate as well as intact *L. sphaericus* wt cells (Figure 1b, Supporting Information Figures S1−S3, and movies S1 and S2).[33] We confirmed that the new material comprised a collection of 2-D crystals with lattice parameters matching the canonical SbpA S-layer. In cryo-ET reconstructions (supporting movie S1) of sufficiently thick regions (200−500 nm), we found mixtures of monolayers and two types of bilayers, often in discotic nematic-like parallel planes (Figure 1c). The bilayers had characteristic intermonolayer distances of either ~13 or ~25 nm (Figure S4). The monolayers comprising the bilayer structures possessed a discrete registry (Figure 1d). Notably, wt SbpA did not form registered bilayers under the same conditions. While the wt protein formed macroscopic films upon centrifugation (in a Ca^{2+}-independent manner), cryo-ET and X-ray scattering analyses revealed these films to comprise randomly stacked 2-D crystals (Figure S5).

We performed high-resolution cryo-ET analysis of rSbpA monolayers by subvolumetric averaging of our

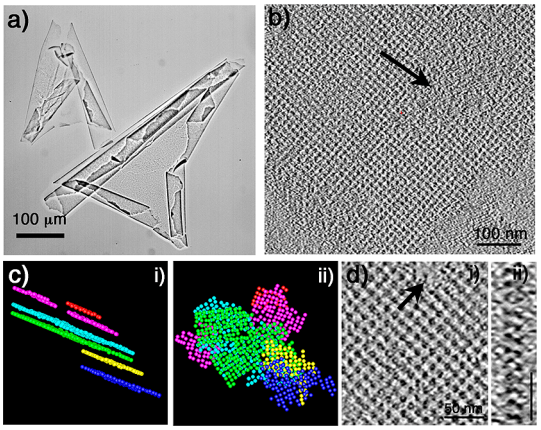

Figure 1. Multiscale assembly of rSbpA leads to crystalline films. (a) Light microscopic image. Crystalline films exhibited various sizes, and large ones tend to wrap around themselves. (b) Slice from a cryo-ET reconstruction of self-assembled films in solution (3 voxels thick average). Black arrows indicate out-of-plane areas of the film, which has smooth undulations when embedded in ice (consistent with observed undulations by Hirn *et al.*[19]). (c) Model representing the 3-D distribution and topology of 2-D crystals within instantly frozen amorphous ice. Each lattice subunit was identified by visual inspection and marked as a sphere, with a different color for each plane. The image shown is a typical example of routinely observed large clusters: (i) side view; (ii) top view. (d) Magnified view of a slice from a 3-D reconstruction subvolume (3 voxels thick average) with in-plane registered lattices: (i) orthogonal slice to (ii) showing the two parallel lattices with a separation of ~13 nm; only one row of lattice subunits is in-plane; see below. The black arrow in (i) points to an area undergoing an onset of disorder and loss of register as the distance between layers increases (*i.e.*, the lattice goes out-of-plane) (scale bar 50 nm).

best data sets (details in Supporting Information).[34] The averaged volume contained a patch of monolayer crystal encompassing nine subunits and provided a detailed view of its lattice and subunit structure (Figure 2 and Figure S6). The overall structure (lattice constant ~13.5 nm) we observed was consistent with Norville and co-workers' previously reported 7 Å 2-D projection map of the wt SbpA S-layer[26] (Figures S6 and S7 for a comparative 2-D projection derived from our data). In addition, our 3-D structure provided new insight into the overall thickness (~18 nm), domain architecture, shape, and orientation of the lattice unit. We identified electron density corresponding to the major (**M**), minor (**m**), and arm (**A**) domains previously identified and named based on their appearance in the 2-D projection.[26,32] Our structure further revealed that the **A** domain actually reflects two distinct regions, which we term the hook (**h**) and loop (**l**) domains; these collapse into overlapping contours in a 2-D electron density map. As Figure 2b shows, all the intersubunit connections within the lattice occur on one face of the S-layer through the **m**, **h**, and **l** domains. The four **M** domains (Figure 2a) of each tetramer create a barrel-like structure that extends to the opposite face of the S-layer. Notably, the rSbpA monolayer structure was highly porous, with the protein occupying only ~18% of each subunit's volume. This suggests a high degree of porosity, which is likely vital for analyte transport in native S-layers and also attractive from the perspective of nanomaterial design.

With an overall structure of the rSbpA S-layer in hand, we sought to further define the regions of the monomer protein that correspond to each face of the 2-D crystal. Such information could provide insight into those forces that promote bilayer formation among rSbpA but not wt SbpA subunits. Previous studies of SbpA S-layers on intact cells have suggested an orientation in which SbpA's C-terminus is exposed on the extracellular face of the 2-D crystal while the N-terminal region of the protein is directly bound to the underlying cell surface.[31,35,36] We therefore analyzed intact *L. sphaericus* cells by cryo-ET with the goal of comparing the native cell-bound S-layer structure to the structure of the rSbpA 2-D crystal shown in Figure 2. Among cells frozen in vitreous ice, we selected those that were oriented approximately parallel to the microscope axis of rotation, far from the cryo-EM grid support film, for imaging analysis. These cells were positioned for cryo-ET reconstructions of their poles, a region where the cell's thickness (~500 and 750 nm) is somewhat lower than its diameter elsewhere (~750 nm to 1 μm). We were able to obtain a low-resolution reconstruction of the S-layer and underlying cell wall covering the poles of the cells, wherein the SbpA lattices were clearly distinguished (Figure 3a and supporting movie S2). The distance from the cytoplasmic membrane to the outer surface of the S-layer was measured to be ~66 nm, while the cell membrane was ~7 nm and the S-layer ~15 nm thick (Figure S3). Interestingly, no periodic arrays were observed in the apex of the cell pole (arrow in Figure 3a). Hundreds of images of S-layer lattices were cropped manually and aligned to define the cubical subvolume of the lattice (Figure 3b). Three orthogonal slices of the averaged reconstruction of the S-layer subunits confirmed both its *p*4 symmetry with a ~13 nm lattice constant and its continuous density through the intersubunit space on the extracellular side (Figure 3c). Four repeating homotetrameric units or "barrels" spanning the S-layer tetragonal lattice were rendered from the selected volume in Figure 3c, corroborating that the cell-bound S-layer structure was clearly related to the rSbpA S-layer structure; they possessed the same lattice parameters, overall subunit shape, and thickness (Figure 3d). The comparison allowed us to assign the orientation of the rSbpA monomers with respect to the overall 2-D crystal lattice. The C-terminal portion of the protein monomer is oriented toward the same face as the **m**, **h**, and **l** domains, while the N-terminal region of the monomer is likely oriented toward the base of the central barrel. Our results also partially confirm, and add molecular details to, previous work by Lepault *et al.*[32] by TEM of negatively stained samples on flat support.

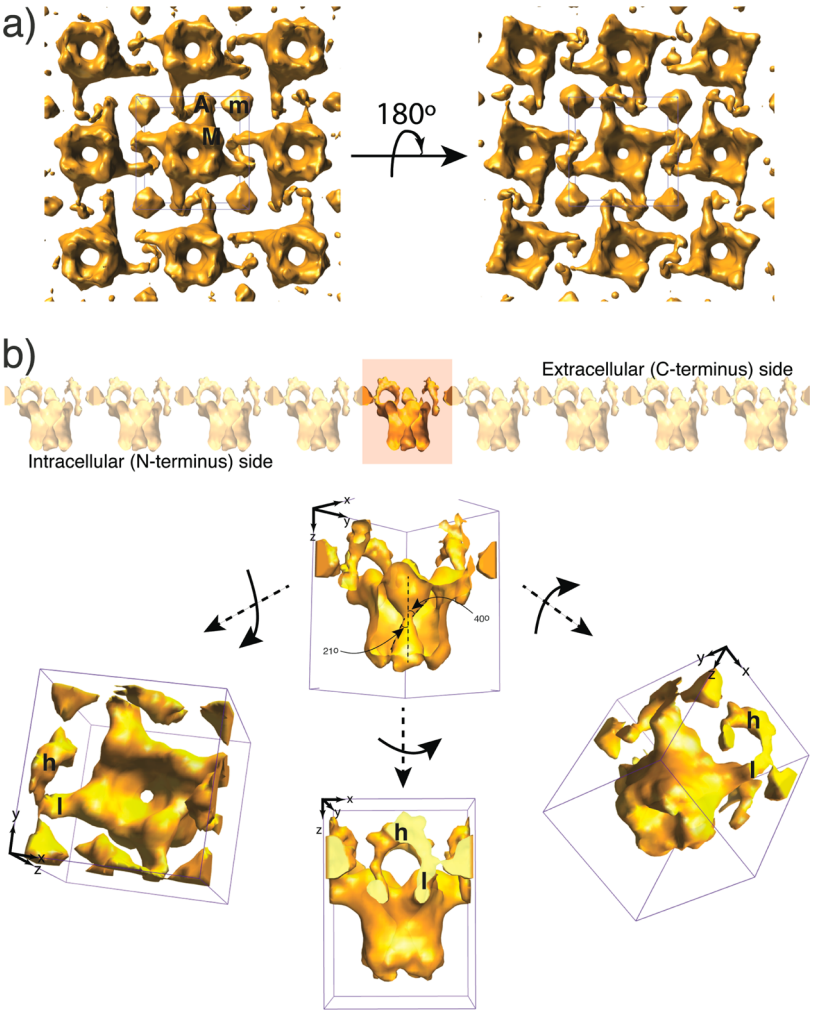

Figure 2. Cryo-ET subtomographic averaged lattice structure reveals anisotropic faces and a porous protein network. (a) Isosurface rendering of the cryo-ET averaged "patch". Boxes in blue define a lattice unit centered on the homotetrameric subunit. (b) Isosurface rendering of the *p*4-symmetric homotetrameric lattice subunit. Four major (M) domains comprise a main body that occupies most of a lattice unit. The hook (h) domain arises from the lower part of the M domain and makes a connection to the loop (l) domain that orients away from the minor (m) domain. The region of contact between the "l" domain and the "m" domain is on the opposite side of the tetramer from l domain. In the z-section image, two narrow, inverted conical channels are connected with angles of 41 and 80° in the middle of the tetramer where a pore of ~2.5 nm diameter is located. The tetrameric protein occupies only ~18% of the subunit volume in these isosurface renderings (see also Supporting Information and Figure S6). Scale: distance between the centers of repeating units is ~13.5 nm.

These include better resolved and accurate 3-D topological relationship between domains, the presence of a central pore in the repeating unit which was uncertain in their work, and the correct height of the near-intact, hydrated S-layers of ~14.6 nm while they reported ~8–9 nm. This is to be expected since negatively stained preparations of macromolecules have consistently shown compression, flattening upon the grid plane, an effect which also changes the spatial relationships between macromolecular domains.[37]

Next, we analyzed the registered bilayers formed during *in vitro* assembly of rSbpA S-layers and confirmed that each monolayer component still maintains its highly ordered architecture, but one is displaced relative to the other (Figure 4a). The bilayers exhibit two characteristic distances between the single layers that were in registry. These distances correspond to two distinct types of contacts between the layers revealed by subtomographic averaging of bilayer patches: the "N-terminus" contact (N–N, (i) of Figure 4b) with a ~13.5 nm distance, and the "C-terminus" contact (C–C, (ii) of Figure 4b) with an average distance of ~25 nm. The direction of the displacement within the crystal plane was very similar in both cases and was aligned with a line connecting the **m** domains diagonally, although the magnitude of the shift was different in the C–C and N–N bilayer: ~2.2 and ~4.9 nm, respectively (Figure 4b,c). The tetramer "barrel" in the N–N bilayer slopes down toward the **m** domain at an angle of ~11°, whereas the tetramer in the C–C bilayer slopes down at a steeper angle. As a result, in each layer in the bilayer structure, the rotational symmetry around the *z*-axis was altered to *p*1 due to the tilt of the homotetramer relative to the normal of the lattice plane (Figure 4b).

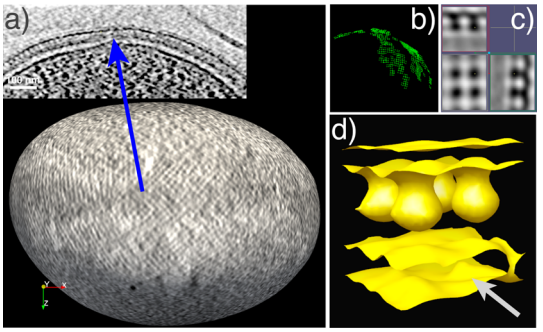

Figure 3. Three-dimensional architecture of the intact cell-bound S-layer (wt SbpA) covering the surface of Lysinibacillus sphaericus by cryo-TE. (a) Three-dimensional cryo-EM reconstructions of intact cells. The main panel is a 1 voxel thick curved surface, or shell, that cuts the S-layer orthogonally to its normal at each point. The inset is a section of a 1 voxel thick slice through the cryo-ET reconstruction of a whole cell, parallel to the main axis. The arrow indicates a region, at the apex of the cell pole, in which the S-layer appears to have no periodic array (in all reconstructions). Scale bar: 100 nm. (b) Manually selected points on the S-layer lattice. (c) Three orthogonal slices through the averaged reconstruction of the S-layer units segmented as outlined in (b). (d) Homotetramer of the S-layer which form the *p*4 lattice, connected through a continuous density "on the outside" of the cell wall (the sheet-like appearance is only due to isosurface rendering constraints: a single contrast value has been chosen; see Figure 2). Between the peptidoglycan (gray arrow) and the S-layer lattice, there is a "gap" of low electron density. We see no order within the layer under the S-layer using the cryo-EM technique.

We further analyzed solutions of the bilayers by synchrotron small-angle X-ray scattering (SAXS) to confirm that the structures determined by cryo-EM were not an artifact of their trapping in vitreous ice. The SAXS spectrum of rSbpA assemblies indicated that the same bilayer structures we observed by cryo-EM were also present in solution (Figure 5a). A comparison of SAXS spectra of rSbpA "S-bilayers" and wt S-layers showed that both proteins form assemblies with the same symmetry and major Bragg peak. However, the spectrum of the rSbpA bilayers possessed a unit cell vector of a = (12.9, 0, 0) nm, b = (0, 12.9, 0) nm, and c = (−5.0, 3.0, 17.5) nm (inset in Figure 5a), whereas the Bragg peaks of the wt S-layer assembly only showed periodicity in-plane (Figure S8). This discrepancy in the Bragg peaks strongly corroborates the formation of a bilayer structure where one layer is shifted with respect to the other in a specific direction (Figure 5b), as hypothesized by Györvary *et al.* in 2003.[38]

In summary, we identified a truncated form of SbpA that forms S-bilayer structures, a starting point for 3-D growth of S-layer crystals. As well, we used cryo-EM and SAXS to define the bilayer structures and also determined the 3-D structure of wt SbpA S-layers on cells.

CONCLUSION

Using whole cell tomograms and 3-D lattice units from *in vitro* rSbpA assemblies, we identified two types of face-to-face interactions originating from the anisotropic

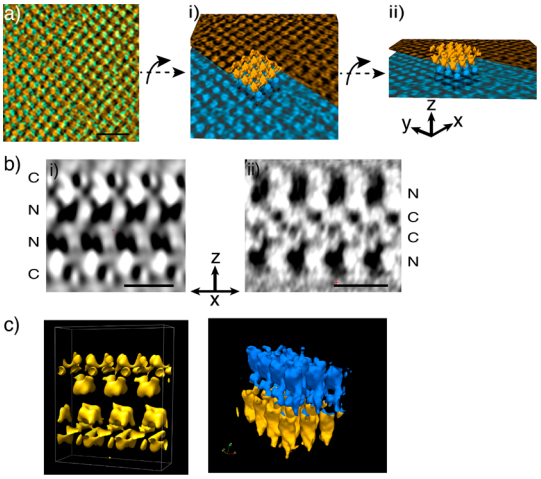

Figure 4. S-bilayers with broken symmetry. (a) Cryo-ET reconstruction of the N−N bilayer. Two false-colored slices through a raw (no averages) 3-D reconstruction with the top and bottom lattices forming the bilayer in-plane with the yellow and blue slicing planes, respectively. (i) Tilted view of the two slices, with an isosurface rendered subtomographic averaged bilayer patch in the center (see full methods in the Supporting Information). The top, yellow slice was cut for visual clarity. (ii) Side view of (i). (b) Orthogonal slice through the bilayer averaged patch. (i) Barrel-like subunits face each other at their N-termini. The dense middle of the N−N bilayer encompassing the barrels is only 24 nm thick. The rotational symmetry around the *z*-axis is broken. The upper layer slides to the orthogonal direction by 4.9 nm, with the tetramer tilted 11° toward the sliding direction. (ii) Orthogonal slice through the bilayer averaged patch of a C−C bilayer crystal. Top layer slides to the orthogonal direction by 2.2 nm, with the tetramer tilted ∼15°. (c) Isosurface rendering of the subtomographic averaged patch. Left, isosurface rendering of a bilayer row, from the subtomographic averaged patch in (a). Right, a tilted view (∼45°) of an isosurface rendered subtomographic averaged patch from the C−C bilayer.

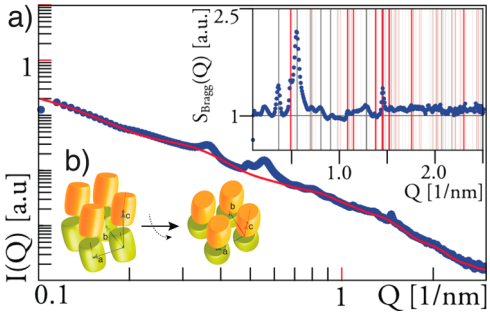

Figure 5. Synchrotron small X-ray scattering spectrum of the rSbpA assembly in solution. (a) Spectrum of the rSbpA sample as a function of the scattering intensity, $I(Q)$. Q is the scattering vector obtained by an equation, $(2/\lambda) \times \sin(\theta/2)$, where λ is the wavelength of incident X-rays and θ is the scattering angle. The orange line indicates the slope, from which the fractal dimension of the system is estimated to be D = 1.9 (see Supporting Information). The red line gives the best fit. In the inset, the vertical lines in red indicate Bragg peaks that can be attributed to the periodicity in-plane, while gray vertical lines indicate Bragg peaks that can be attributed to contributions perpendicular to the plane. (b) Model of a unit cell in the bilayer structure. Each cylinder represents a tetramer whose different colors show two registered layers. The arrows are vectors that define a unit cell; a = (12.9, 0, 0) nm, b = (0, 12.9, 0) nm, c = (−5.0, 3.0, 17.5) nm.

faces of the crystal; these interactions are absent in wt SbpA S-layers. In the S-bilayers, both the broken symmetry and the direction of monolayer displacement strongly suggest that the C-terminus contributes to the association of four **m** domains and its truncation in rSbpA destabilizes their interaction. The propensity of rSbpA to form bilayers may reflect altered C-terminal topography and charge distribution that promote stability of the 3-D structure.

The stable formation of S-bilayer structures suggests the potential for utilizing S-layer proteins as building blocks in hierarchical 3-D nanostructure assembly. It may be possible to further engineer these proteins to achieve more extended arrays with order in the third dimension. One might also be able to build new structures directly from S-bilayer intermediates. The structural information we acquired in this work may also facilitate genetic engineering of new S-layer protein interactions because we now have a more clear understanding of the 3-D positioning of the SbpA protein domains. More detailed structural information would be required to guide high-precision genetic engineering of new S-layer architectures, but the findings reported here represent a critical first step toward achieving this goal.

METHODS

Cryo-TEM Samples. For cryo-TEM, aliquots of 5 μL were taken directly either from fresh cell cultures or *in vitro* assembled samples, placed onto lacey carbon grids (Ted Pella, INC, #01881), and cryo-plunged. Images were acquired on a JEOL-3100 FFC electron microscope equipped with a field emission gun (FEG) electron source operating at 300 kV, an Omega energy filter, and a cryo-transfer stage. Images were recorded on a Gatan 795 2K $\times$ 2K CCD camera or on a Gatan 795 4k $\times$ 4k CCD camera mounted at the exit of an electron decelerator operated at 248 kV, resulting in images formed by a 52 kV electron beam at the CCD (see also Supporting Information). For data acquisition, the program Serial-EM (http://bio3d.colorado.edu/) adapted to JEOL microscopes was used, and reconstructions were obtained with the program Imod (http://bio3d.colorado.edu/).

Cryo-TEM Data. For final analysis and presentation, we chose two cryo-ET reconstructions of intact *Lysinibacillus sphaericus* cells and seven of the *in vitro* reconstituted samples, obtained using the 2K $\times$ 2K camera with sampling 1.2 and 0.68 nm/pixel and defocus $\sim$12.0 and $\sim$6.4 μm, respectively. For the final highly resolved reconstructions, we selected four data sets of the *in vitro* system obtained with a decelerator-coupled 4k $\times$ 4k CCD, using a defocus of $\sim$3.4 μm and with pixel size 3.75 Å (details in Supporting Information).

Image Processing and Analyses. All tomographic reconstructions were obtained with the program Imod (http://bio3d.colorado.edu/). The program ImageJ (NIH, http://rsb.info.nih.gov/ij/) was used for analysis of the 2-D image projections. Volume rendering and image analysis of tomographic reconstructions were performed using the program Paraview (http://www.paraview.org) and Chimera (http://www.cgl.ucsf.edu/chimera/). All movies were generated with the package ffmpeg (www.ffmpeg.org). Cell surfaces containing the S-layer lattice were segmented by hand with Imod. Then these segmented surface models were converted to a smooth triangular mesh in The Visualization Toolkit (VTK, www.vtk.org) by a custom-built code. The final gray scale values on the curved surface display (Figure 3a and supporting movie 2) were obtained by computing, at each point, the average of five gray scale values along the normal to the surface: two below, two above the surface, and one on the surface. These intact cell surfaces were used as visual aids for the hand selection of S-layer units using imod; see below.

Classification, Alignment, and Averaging of Subtomographic Volumes. S-layers on whole cells, *in vitro* reconstituted monolayers, and bilayer crystals were used for testing, trouble-shooting, and improving the development of an algorithm for the alignment and averaging of cryo-ET subvolumes: thresholded constrained cross-correlation (TCCC) (http://www-vlsi.stanford.edu/TEM/software.html).[34] For more details on cryo-ET missing wedge and subvolumetric averaging, see Amat *et al.*[17,34] and references therein. All classification, alignment, and averaging of subtomographic volumes were done with TCCC and with Bsoft (NIH, http://lsbr.niams.nih.gov/bsoft/) for comparison.

Whole cell reconstructions were surveyed with Imod, and the locations of 640 S-layer lattice units were manually chosen and stored in a segmented model (Figure 3b). Cubical subvolumes, with assigned normals pointing outward from the cell surface, were cropped. The side of the cubical volume was about twice the lattice constant and contained a centered repeating unit. The center of each repeating unit in the subvolume was aligned for averaging 3-D S-layer lattices. This process allowed computation of the center of mass of each cropped subvolume and use of a cell surface normal at each point for rotational alignment of all subvolumes. In whole cell data, the normal defines the outside of the bacterium and allows the merging of data from different cryo-tomograms. The large defocus value used for whole cell data ($\sim$12 μm) was consistent with the sampling resolution limit imposed by large cell sizes, but these factors limit our analysis.

All volumes were cropped by direct visual inspection with Bsoft (NIH, http://lsbr.niams.nih.gov/bsoft/) and TCCC[34] in 3-D boxes more than twice the size of the S-layer tetramers ($\sim$37 nm by side). In the self-assembled *in vitro* samples, the normal to the surface defined the two sides of the lattices: C-terminus or N-terminus.

Preliminary 3-D alignment and averaging of S-layer subvolumes were performed with four data sets that were obtained from the *in vitro* samples (2K $\times$ 2K camera), and these data sets were also used to analyze the bilayer structures. First, approximately 2100 boxes (61 voxels or $\sim$41 nm by side) with oriented normal centered by the homotetramer were manually chosen using Imod from these cryo-ET 3-D reconstructions. From selected regions of the same data, within the correlated C$-$C bilayer lattices, 553 boxes (119 voxels or $\sim$81 nm by side) centered on pairs of in-register subunits (octamers: dimers of homotetramer) were also chosen manually using Imod (Figure S4). For the N$-$N bilayer lattices, three additional data sets were used, from which approximately 406 boxes (119 voxels or $\sim$81 nm by side) were centered by pairs of registered subunits and were chosen for final alignment and averaging from regions of correlated bilayer lattices. Each bilayer lattice structure is not uniform due to a variable distance between each layer (Figure S4). The distances in the C$-$C bilayer are more variable than those in the N$-$N bilayer. The final reconstruction of an N$-$N bilayer "patch" shown in Figure 4c was computed using a subset of 346 subvolumes. The averaged reconstructions of the monolayer lattices were used as initial models to perform the iterative classification, alignment, and averaging for higher-resolution data. In a second step, approximately 3100 3-D particles or boxes (119 voxels or $\sim$44.6 nm, by side) were hand selected and cropped from four reconstructions obtained with the 4k $\times$ 4k decelerator-coupled CCD as described above. All alignments and averages were done using TCCC;[34] part of the data was processed using the various programs within Bsoft for control purposes.

Conflict of Interest: The authors declare no competing financial interest.

Acknowledgment. We thank Virginia Altoe for TEM of the stained sample, and Eric Schaible for helping the beamline experiment. This work was performed at Lawrence Berkeley

National Laboratory, with support from the Office of Science, Office of Basic Energy Sciences, Biological and Environmental Research, of the U.S. Department of Energy under Contract No. DE-AC02-05CH11231.

Supporting Information Available: Description of DNA plasmid preparation, the protein expression and purification, images and their analysis of atomic force microscopy and transmission electron microscopy, experimental details, and analysis of synchrotron small-angle X-ray scattering. This material is available free of charge *via* the Internet at http://pubs.acs.org.

REFERENCES AND NOTES

1. Sleytr, U. B.; Huber, C.; Ilk, N.; Pum, D.; Schuster, B.; Egelseer, E. M. S-Layers as a Tool Kit for Nanobiotechnological Applications. *FEMS Microbiol. Lett.* **2007**, *267*, 131–144.
2. Tang, J.; Badelt-Lichtblau, H.; Ebner, A.; Preiner, J.; Kraxberger, B.; Gruber, H. J.; Sleytr, U. B.; Ilk, N.; Hinterdorfer, P. Fabrication of Highly Ordered Gold Nanoparticle Arrays Templated by Crystalline Lattices of Bacterial S-Layer Protein. *ChemPhysChem* **2008**, *9*, 2317–2320.
3. Sierra-Sastre, Y.; Choi, S.; Picraux, S. T.; Batt, C. A. Vertical Growth of Ge Nanowires from Biotemplated Au Nanoparticle Catalysts. *J. Am. Chem. Soc.* **2008**, *130*, 10488–10489.
4. Mark, S. S.; Bergkvist, M.; Yang, X.; Teixeira, L. M.; Bhatnagar, P.; Angert, E. R.; Batt, C. A. Bionanofabrication of Metallic and Semiconductor Nanoparticle Arrays Using S-Layer Protein Lattices with Different Lateral Spacings and Geometries. *Langmuir* **2006**, *22*, 3763–3774.
5. Mark, S. S.; Bergkvist, M.; Bhatnagar, P.; Welch, C.; Goodyear, A. L.; Yang, X.; Angert, E. R.; Batt, C. A. Thin Film Processing Using S-Layer Proteins: Biotemplated Assembly of Colloidal Gold Etch Masks for Fabrication of Silicon Nanopillar Arrays. *Colloid Surf., B* **2007**, *57*, 161–173.
6. Douglas, K.; Devaud, G.; Clark, N. A. Transfer of Biologically Derived Nanometer-Scale Patterns to Smooth Substrates. *Science* **1992**, *257*, 642–644.
7. Schuster, D.; Kupcu, S.; Belton, D. J.; Perry, C. C.; Stoger-Pollach, M.; Sleytr, U. B.; Pum, D. Construction of Silica-Enhanced S-Layer Protein Cages. *Acta Biomater.* **2013**, *9*, 5689–5697.
8. de la Rica, R.; Matsui, H. Applications of Peptide and Protein-Based Materials in Bionanotechnology. *Chem. Soc. Rev.* **2010**, *39*, 3499–3509.
9. Papapostolou, D.; Howorka, S. Engineering and Exploiting Protein Assemblies in Synthetic Biology. *Mol. BioSyst.* **2009**, *5*, 723–732.
10. Sarikaya, M.; Tamerler, C.; Schwartz, D. T.; Baneyx, F. O. Materials Assembly and Formation Using Engineered Polypeptides. *Annu. Rev. Mater. Res.* **2004**, *34*, 373–408.
11. Sleytr, U. B.; Schuster, B.; Egelseer, E. M.; Pum, D.; Horejs, C. M.; Tscheliessnig, R.; Ilk, N. Nanobiotechnology with S-Layer Proteins as Building Blocks. *Prog. Mol. Biol. Transl. Sci.* **2011**, *103*, 277–352.
12. Koudelka, K. J.; Manchester, M. Chemically Modified Viruses: Principles and Applications. *Curr. Opin. Chem. Biol.* **2010**, *14*, 810–817.
13. Soto, C. M.; Ratna, B. R. Virus Hybrids as Nanomaterials for Biotechnology. *Curr. Opin. Biotechnol.* **2010**, *21*, 426–438.
14. Fischlechner, M.; Donath, E. Viruses as Building Blocks for Materials and Devices. *Angew. Chem., Int. Ed.* **2007**, *46*, 3184–3193.
15. Bernards, D. A.; Desai, T. A. Nanoscale Porosity in Polymer Films: Fabrication and Therapeutic Applications. *Soft Matter* **2010**, *6*, 1621–1631.
16. DuFort, C. C.; Dragnea, B. Bio-Enabled Synthesis of Metamaterials. *Annu. Rev. Phys. Chem.* **2010**, *61*, 323–344.
17. Amat, F.; Comolli, L. R.; Nomellini, J. F.; Moussavi, F.; Downing, K. H.; Smit, J.; Horowitz, M. Analysis of the Intact Surface Layer of *Caulobacter crescentus* by Cryo-Electron Tomography. *J. Bacteriol.* **2010**, *192*, 5855–5865.
18. Smit, J.; Engelhardt, H.; Volker, S.; Smith, S. H.; Baumeister, W. The S-Layer of *Caulobacter crescentus*: Three-Dimensional Image Reconstructure and Structure Analysys by Electron Microscopy. *J. Bacteriol.* **1992**, *174*, 6527–6538.
19. Hirn, R.; Schuster, B.; Sleytr, U. B.; Bayerl, T. M. The Effect of S-Layer Protein Adsorption and Crystallization on the Collective Motion of a Planar Lipid Bilayer Studied by Dynamic Light Scattering. *Biophys. J.* **1999**, *77*, 2066–2074.
20. Baranova, E.; Fronzes, R.; Garcia-Pino, A.; Van Gerven, N.; Papapostolou, D.; Pehau-Arnaudet, G.; Pardon, E.; Steyaert, J.; Howorka, S.; Remaut, H. SbsB Structure and Lattice Reconstruction Unveil Ca^{2+} Triggered S-Layer Assembly. *Nature* **2012**, *487*, 119–122.
21. Ballister, E. R.; Lai, A. H.; Zuckermann, R. N.; Cheng, Y.; Mougous, J. D. *In Vitro* Self-Assembly from a Simple Protein of Tailorable Nanotubes Building Block. *Proc. Natl. Acad. Sci. U.S.A.* **2008**, *105*, 3733–3738.
22. Padilla, J. E.; Colovos, C.; Yeates, T. O. Nanohedra: Using Symmetry To Design Self Assembling Protein Cages, Layers, Crystals, and Filaments. *Proc. Natl. Acad. Sci. U.S.A.* **2001**, *98*, 2217–2221.
23. Fegan, A.; White, B.; Carlson, J. C. T.; Wagner, C. R. Chemically Controlled Protein Assembly: Techniques and Applications. *Chem. Rev.* **2010**, *110*, 3315–3336.
24. Carlson, J. C. T.; Jena, S. S.; Flenniken, M.; Chou, T. F.; Siegel, R. A.; Wagner, C. R. Chemically Controlled Self-Assembly of Protein Nanorings. *J. Am. Chem. Soc.* **2006**, *128*, 7630–7638.
25. Ringler, P.; Schulz, G. E. Self-Assembly of Proteins into Designed Networks. *Science* **2003**, *302*, 106–109.
26. Norville, J. E.; Kelly, D. F.; Knight, T. F.; Belcher, A. M.; Walz, T. 7 Angstrom Projection Map of the S-Layer Protein SbpA obtained with Trehalose-Embedded Monolayer Crystals. *J. Struct. Biol.* **2007**, *160*, 313–323.
27. Chung, S.; Shin, S.-H.; De Yoreo, J. J.; Bertozzi, C. R. Self-Catalyzed Growth of S-Layers *via* an Amorphous-to-Crystalline Transition Limited by Folding Kinetics. *Proc. Natl. Acad. Sci. U.S.A.* **2010**, *107*, 16536–16541.
28. Aebi, U.; Smith, P. R.; Dubochet, J.; Henry, C.; Kellenberger, E. A Study of the Structure of the T Layer of *Bacillus-brevis*. *J. Supramol. Struct.* **1973**, *1*, 498–522.
29. Huber, C.; Ilk, N.; Runzler, D.; Egelseer, E. M.; Weigert, S.; Sleytr, U. B.; Sara, M. The Three S-Layer-like Homology Motifs of the S-Layer Protein SbpA of *Bacillus sphaericus* CCM 2177 Are Not Sufficient for Binding to the Pyruvylated Secondary Cell Wall Polymer. *Mol. Microbiol.* **2005**, *55*, 197–205.
30. Sleytr, U. B.; Sara, M.; Pum, D.; Schuster, B. Characterization and Use of Crystalline Bacterial Cell Surface Layers. *Prog. Surf. Sci.* **2001**, *68*, 231–278.
31. Ilk, N.; Vollenkle, C.; Egelseer, E. M.; Breitweiser, A.; Sleytr, U. B.; Sara, M. Molecular Characterization of the S-Layer Gene, SbpA, of *Bacillus sphaericus* CCM 2177 and Production of a Functional S-Layer Fusion Protein with the Ability To Recrystallize in a Defined Orientation while Presenting the Fused Allergen. *Appl. Microbiol.* **2002**, *68*, 3251–3260.
32. Lepault, J.; Martin, N.; Leonard, K. 3-Dimensional Structure of the T-Layer of *Bacillus sphaericus* P-1. *J. Bacteriol.* **1986**, *168*, 303–308.
33. Friedrich, H.; Frederik, P. M.; de With, G.; Sommerdijk, N. A. Imaging of Self-Assembled Structures: Interpretation of TEM and Cryo-TEM Images. *Angew. Chem., Int. Ed.* **2010**, *49*, 7850–7858.
34. Amat, F.; Comolli, L. R.; Moussavi, F.; Smit, J.; Downing, K. H.; Horowitz, M. Subtomogram Alignment by Adaptive Fourier Coefficient Thresholding. *J. Struct. Biol.* **2010**, *171*, 332–344.
35. Ilk, N.; Kosma, P.; Puchberger, M.; Egelseer, E. M.; Mayer, H. F.; Sleytr, U. B.; Sara, M. Structural and Functional Analyses of the Secondary Cell Wall Polymer of *Bacillus sphaericus* CCM 2177 That Serves as an S-Layer-Specific Anchor. *J. Bacteriol.* **1999**, *181*, 7643–7646.
36. Mesnage, S.; Fontaine, T.; Mignot, T.; Delepierre, M.; Mock, M.; Fouet, A. Bacterial SLH Domain Proteins Are Non-covalently Anchored to the Cell Surface *via* a Conserved Mechanism Involving Wall Polysaccharide Pyruvylation. *EMBO J.* **2000**, *19*, 4473–4484.

37. Frank, J. *Three-Dimensional Electron Microscopy of Macromolecular Assemblies: Visualization of Biological Molecules in Their Native State*; Oxford University Press: New York, 2006; Chapters 1−4.
38. Gyorvary, E. S.; Stein, O.; Pum, D.; Sleytr, U. B. Self-Assembly and Recrystallization of Bacterial S-Layer Proteins at Silicon Supports Imaged in Real Time by Atomic Force Microscopy. *J. Microsc.* **2003**, *212*, 300–306.